Plasma Sources Science and Technology

PURPOSE-LED PUBLISHING™

PAPER • **OPEN ACCESS**

2D imaging of atomic oxygen reaction dynamics after a nanosecond pulse discharge using Light-field Amplitude Control

To cite this article: Jonas Ravelid *et al* 2025 *Plasma Sources Sci. Technol.* **34** 105010

OPEN ACCESS
IOP Publishing
Plasma Sources Science and Technology
Plasma Sources Sci. Technol. **34** (2025) 105010 (13pp)
https://doi.org/10.1088/1361-6595/ae0760

2D imaging of atomic oxygen reaction dynamics after a nanosecond pulse discharge using Light-field Amplitude Control

Jonas Ravelid, Jinguo Sun, Vassily Kornienko, Alexander A Konnov, Elias Kristensson, Yupan Bao and Andreas Ehn*

Combustion Physics, Department of Physics, Lund University, Box 118, SE-221 00 Lund, Sweden

E-mail: andreas.ehn@fysik.lu.se

Received 6 December 2024, revised 28 June 2025
Accepted for publication 16 September 2025
Published 10 October 2025

Abstract

Plasma-assisted technologies are rapidly advancing and are set to play a crucial role in the green transition. One challenge in this development, specifically tied to laser-based plasma diagnostics, is the presence of interfering plasma-induced emissions, such as the de-excitation of naturally excited species, which can complicate the detection of laser-induced signals. Successfully differentiating between the two would unlock new measurement possibilities within plasma and its applications. This paper presents an adaptation of light-field amplitude control (LAC), a novel approach to two-photon atomic laser-induced fluorescence (LIF), which effectively separates LIF from plasma emissions. We demonstrate this capability by distinguishing between plasma emission and LIF in the afterglow of a nanosecond pulsed discharge in atmospheric pressure oxygen gas. Utilising LAC, we present single-shot 2D maps of ground state atomic oxygen distributions at different delays after discharge. Additionally, we report on the temporal dynamics of ground-state atomic oxygen concentration following the discharge, quickly growing until peaking at 2.8 μs, information that was previously unavailable due to interfering plasma emissions. We have also analysed the consumption of atomic oxygen, presenting a 2D map of consumption dynamics and chemical lifetime. Directly, these results will lead to a better understanding of plasma chemistry in oxygen gas, especially the rapid growth phase, but the adaptation of LAC to general plasma diagnostics will enable the extraction of a whole host of new information through the removal of plasma emission.

Supplementary material for this article is available online

keywords: nanosecond pulsed discharge, atomic oxygen, plasma emission removal, TALIF, temporal dynamics, lifetime, Fourier filtering

* Author to whom any correspondence should be addressed.

1. Introduction

As our society attempts the largest infrastructure overhaul in history with the green transition, plasma has been identified and demonstrated as a promising technology to support this process [1]. Plasma-based technologies have shown significant promise in applications such as bio-fuel production [2, 3], improving crop yield and food production [4], reforming greenhouse gases into usable chemicals and fuels [5–7], and assisting in ignition and combustion control [8–11], all areas that require improvement for a sustainable future. These processes rely on plasma's ability to generate reactive species and induce complex chemical transformations, but the precise mechanisms by which plasma contributes to these processes are not fully understood. Moreover, plasma encompasses a wide range of ionised gases, each characterised by varying temperatures, densities, energy distributions, and levels of ionisation. To fully harness plasma's potential, there is a need for advanced analysis and diagnostic tools capable of accurately characterising its spatial and temporal properties.

While thermal plasma provides excellent heating opportunities due to high-energy ions, non-thermal plasma has been identified as more chemically useful due to its ability to initiate chemical reactions through electron interaction without excess energy loss due to heating of ions [12]. The interaction between high-speed electrons and a chemical system can then be utilised to initiate, sustain or alter reaction pathways. One way to achieve non-thermal plasma effects is to apply high voltage in short pulses. The pulsed electric field generates high-temperature electrons, while keeping the ion temperature low due to the considerable difference in rest mass. The effect of applying a short high voltage pulse can be observed tens of milliseconds later, despite the pulse itself lasting down to a few nanoseconds (ns).

Studying the effects of pulsed discharge plasma is essential for understanding the mechanisms behind plasma-assisted processes, and its potential applications. The effect of applied plasma depends on the properties of the plasma, which tend to vary both spatially and temporally (especially for pulsed plasma), making plasma-based processes challenging to evaluate. Despite this, plasma-produced atomic oxygen (O) is of significant interest due to its vital role in wide range of applications. O plays a crucial role in processes such as semiconductor chip etching [13], biomedical sterilisation [14], and the controlled modification of polymer surfaces [15]. Additionally, O is central to various oxidation reactions [16], making the plasma-induced dissociation of molecular oxygen (O_2) a key area of study.

As stated, chemical effects in the vicinity of a discharge channel can vary widely due to local properties of the plasma, and an analytical method that can resolve these transient dynamic distributions is required. Such a method should also be non-intrusive so that the measurement itself does not compromise the integrity of the results. One option for plasma diagnostics that fulfils these requirements is laser-induced fluorescence (LIF), a widely used scientific tool in not only physics and chemistry [17] but also medicine [18] and industrial chemical processing [19]. Beyond spatial and temporal resolution capability, it has increasingly gained momentum in plasma diagnostics due to its ability to target individual species in the plasma. It also produces fluorescence signal at known wavelengths with a high signal-to-noise ratio compared to many other diagnostic techniques [20]. Furthermore, if a sufficiently powerful laser is used, the laser beam can be expanded into a vertical 2D sheet, often referred to as Planar LIF or PLIF. The 2D sheet means that a two-dimensional cross-section of the target can be imaged and spatial distributions can be probed.

However, investigating atomic species and smaller radicals, such as O, H, and CO remains a challenge. Such radicals have electronic transitions from the ground state that require excitation in the vacuum ultra-violet range, something that is very challenging to achieve at atmospheric gas composition and pressure. To overcome this, two-photon atomic LIF (TALIF) can be employed, where two photons of lower energy are used for excitation. However, the absorption cross-section for two-photon excitation is orders of magnitude weaker than its single-photon equivalent, which leads to very weak fluorescence signal. The two-photon fluorescence intensity scales quadratically with photon flux on the other hand, making the use of ultrafast lasers, which provide laser pulses with extreme photon flux, highly advantageous. The rapid development of such laser systems over the last decade has also enabled single-shot planar TALIF 2D imaging measurements, albeit until recently limited to small sheets on the order of a few millimetres [21].

Consequently, TALIF of O has been performed in a large variety of plasma-related measurement schemes, including plasma jets [22, 23], microwave discharges [24] and ns-pulse discharges [25–28], in conjunction with simulation efforts [29–31]. However, one thing common to all this experimental data is that the data was either (a) produced in gas with relatively small fractions of O_2, or (b) taken well after the end of the afterglow phase, likely due to significant interfering emission from de-excitation of plasma-excited O. The vast majority are also not imaging- but point measurements, thus lacking information on spatial variations. Consequently, there are a few published articles on O dynamics in the presence of other gases but virtually no information about the dynamics of O in O_2 gas, especially spatially resolved. What little information exists is acquired long after the end of the afterglow phase.

This is because the plasma-induced emission, henceforth called plasma emission, is spatially, temporally, and often spectrally, indistinguishable from the laser-induced florescence so there is no way to separate one from the other. This is true not only for O, in general it is extremely challenging to capture distributions and dynamics of intermediate reactive species with TALIF if there is a luminous plasma afterglow. A way to distinguish between LIF and plasma emissions is thus needed.

Over the last decade, diagnostic adaptations based on image- and Fourier analysis [32, 33] have gained traction as it has been shown to be able to suppress stray light [34] or even separate spectral components entirely [35], enabling snapshot

multi-spectral imaging. The basic principle of structured illumination with PLIF is to illuminate an object with a striped pattern instead of a homogeneous laser sheet. This results in a modulated fluorescence signal distribution that can be isolated from any unmodulated interfering background that is not laser-induced through band-pass filtering in the Fourier domain. For plasma-diagnostic purposes, Fourier analysis was recently used to indirectly image spatial CH_3 distributions in a DBD plasma cell by laser-induced photolytic breakdown into CH. The CH was then imaged using PLIF and Fourier filtering used to distinguish between laser-created CH and naturally occurring CH [36].

This paper presents light-field amplitude control (LAC), a technique based of Fourier analysis previously shown to vastly improve results from Planar TALIF measurements of ground state atomic oxygen (O(3P)) in a flame [37]. In this adaptation of LAC we theoretically sacrifice $\frac{3}{8}$ of the fluorescence signal to distinguish between laser-induced signal and plasma emission. It should be noted, however, that despite this reduction in signal, we still achieve a signal improvement of 125% compared to planar laser illumination. The Fourier-filtering then allows distinction between plasma emissions and LIF, removing a major hurdle for investigating plasma chemistry in the afterglow. We demonstrate its application on plasma resulting from a high-voltage ns pulsed discharge (NPD) generated at atmospheric pressure in pure oxygen gas (O_2), evaluating and showcasing its ability to accurately remove plasma emission in both single-shot and accumulated datasets, through the application of Lock-in analysis to the spatial modulation. LA C+ Lock-in also pushes the limit for how early after the discharge information can be extracted by over 2 μs, revealing a previously inaccessible creation phase of O(3P). We investigate O(3P) fluorescence intensity in the plasma channel up to 500 μs after the NPD, resulting in an average chemical lifetime characterisation. Finally, we present 2D maps of fluorescence over time after discharge, as well as a pixel-wise calculated lifetime map, showcasing the spatio-temporal behaviour of O(3P).

2. Methods

2.1. Experimental setup

A depiction of the experimental setup is displayed in figures 1(a) and (b). The setup involved applying NPD-induced plasma to O_2 flowing between between a porous plug and a flow stabilisation plate. The porous plug featured two outlets, a central circular outlet (60 mm diameter) that flowed O_2 while the outer ring (15 mm width, for a total outer diameter of 90 mm) flowed N_2, serving to shield the inner gas flow from external gas movement. Gas flow rates were maintained at 12 l^{-1} min O_2 and 15 l^{-1} min N_2, resulting in a matched flow velocity for both gases of 71 mm s^{-1}. The flow stabilisation plate was located approximately 17 mm above the porous plug.

The plasma was generated in a pin-to-pin electrode configuration with conical stainless steel pins, with both height and diameter of 4 mm. The bottom pin (cathode) was placed at the centre of the porous plug, connected to ground, while the top pin (anode) was fastened below the stabilisation plate, connected to a FPG200-1NM1 High Voltage Pulse Generator. The pulse generator produces <3 ns duration positive bias pulses of 30 kV at 5 Hz when matching into a 75 Ω impedance. The actual impedance in the pin-to-pin configuration is much higher, affecting the duration of the discharge pulse in the experiment. The gap between the pins was 9 mm, chosen because it was the largest gap that in practice reliably produced spark discharges. The voltage and current were monitored using voltage and current probes: Tektronix P6015A and Pearson 6585, respectively. Typical *I–V* curves for the NPD are displayed in figures 1(c) and (d). Calculating the energy deposition from the *I–V* curves gives a total energy deposition of 170 ± 20 mJ. Assuming a 9 mm high discharge column with 0.5 mm radius yields a specific energy input of 24 ± 3 mJ mm^{-3}.

The matched flow velocity was confirmed to completely exchange the gas in the discharge volume, leaving no detectable O_3 or temperature elevations from one discharge to the next, when operating the discharge at 5 Hz.

2.2. Optical diagnostics setup

The O(3P) atoms were probed using laser radiation from a femtosecond laser (Ekspla UltraFlux FT405-LLC). The laser system generates pulses at 5 Hz with a duration of 35 fs at a wavelength of 225.3 nm (spectral bandwidth 2.4 nm full width at half maximum (FWHM)), delivering 33 μJ of pulse energy just after the probe volume. The O(3P) excitation scheme is displayed in figure 1(e).

A cylindrical lens focused the light into a vertical sheet, which produced the O(3P) fluorescence. The spatial sheet modulation was achieved using a DOE, which first split the laser pulse into two diverging components. A second cylindrical lens refocused them in the probe volume, which produced the LAC modulation through interference between the two components where they overlap, see figure 1(b) (Consequently, any fluorescence image not post-processed will display the LAC-based modulation). The sheet dimensions at the beam waist was estimated to 9×0.2 mm, with a Rayleigh range of 18 mm. This gives a maximum irradiance of 1.06×10^{11} W cm^{-2} when accounting for the modulation, just at the limit for quadratic regime, interference-free TALIF of O at atmospheric pressure set by Rahman *et al* [38].

An intensified sCMOS camera (ANDOR iSTAR with VIH photo-cathode type), equipped with a 50 mm objective (NIKKOR F/1.2) and a band-pass filter transmitting light between 840 and 850 nm, was placed perpendicular to the laser sheet, detecting the spatial O(3P) fluorescence distribution. It imaged the fluorescence distribution from the O(3P) atoms with a camera gate-width of 4 ns.

The triggering scheme for plasma generation, laser and camera was designed to allow the laser to probe the O(3P) atom distribution at variable times after the NPD. This setup enabled the study of 2D O(3P) chemical lifetime by imaging O(3P) distributions at different delays following the NPD across multiple discharge pulses. For each delay, data consisted of 50 single-shot images, from which average

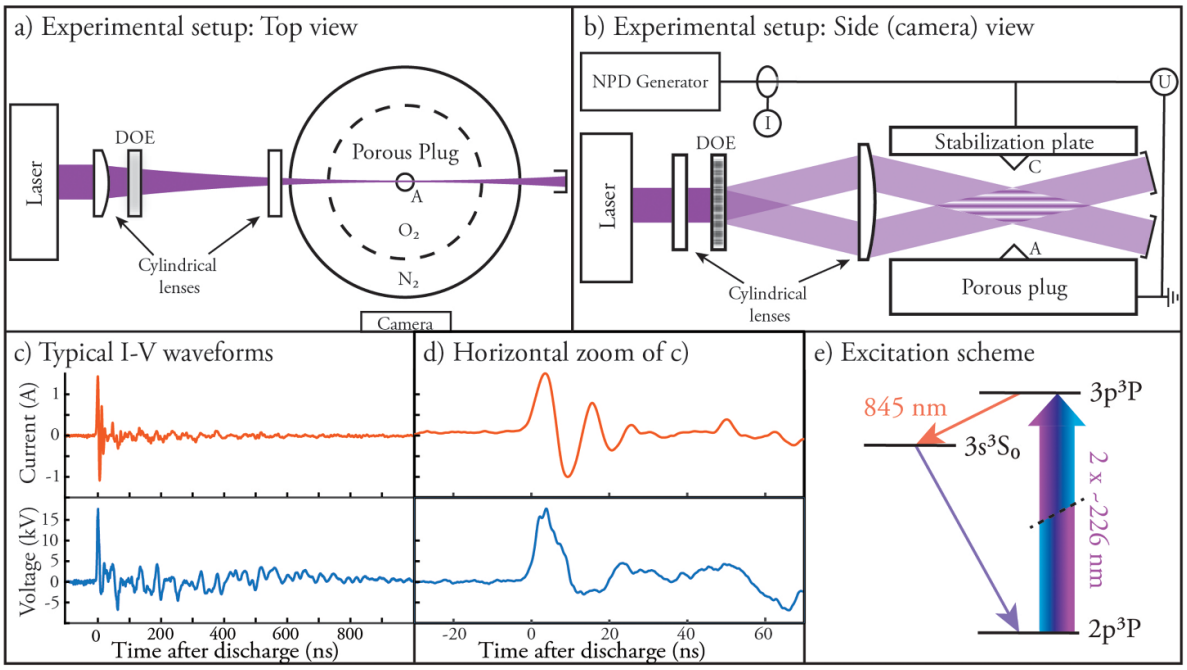

Figure 1. (a) and (b) Displays the experimental setup, with optics enabling LAC. The positive-bias NPD generator is connected to the pin electrode under the stabilising plate. The porous plug, which the gas is flown through, is grounded. The first cylindrical lens forms the laser pulses into vertical sheets. The diffractive optical element (DOE) splits the pulses into two diverging components, which are redirected and made to overlap by the second cylindrical lens, creating a sinusoidal modulation pattern in the volume of overlap. (c) Shows typical voltage and current wave forms for the NPD and (d) shows a zoom in the temporal domain around the discharge. (e) displays the excitation scheme used for O(3P) fluorescence.

datasets were produced. Compensation for inhomogeneities in the laser sheet was achieved using fluorescence data from a homogeneous distribution of xenon gas.

Initially, the goal was to achieve calibration for absolute number density measurements in a similar manner to [39] but due to technical constraints a 1:1 map between Xe and O(3P) fluorescence was impossible with on-resonance excitation for both species. Instead, the wide bandwidth of the laser pulse (2.5 nm FHWM) was utilised to excite both species slightly off-resonance. The consequence of this is that while laser profile corrections could be made, the correlation of absolute density to fluorescence signal becomes non-trivial, especially since this would be coupled with pixel-wise calculated fluorescence lifetimes with very high uncertainties. However, since all steps in the Lock-in Fourier filtering process are linear operations, there is nothing theoretically hindering the use of LAC when achieving absolute number density measurements.

An alternative calibration method involves a low-pressure discharge cell containing a known O_2/N_2 gas mixture, as presented by Shu *et al* [40]. By assuming complete dissociation of O_2 in the plasma, the resulting atomic oxygen density can be treated as known, allowing absolute TALIF calibration without the need for off-resonance normalisation. While effective for ns and picosecond excitation, this method becomes incompatible with ultrashort-pulse excitation due to the significant group delay dispersion introduced by the cell's optical windows. For example, 1 mm-thick fused silica windows induce enough chirp to severely degrade pulse compression and two-photon excitation efficiency for sub-100 fs pulses. As a result, such a calibration approach is unsuitable when using femtosecond pulses. Further analysis is provided in the supplementary material.

In this setup, two photons at around 225.65 nm were used to excite O, leading to de-excitation via the emission of a fluorescence photon at 844.6 nm, which can be detected by a camera sensitive in the near-infrared range. In applications where O_3 is produced, using UV photons for excitation presents challenges, as these photons can photolytically dissociate O_3 into additional O atoms. However, the ultrafast femtosecond-duration pulses used in this study are sufficiently brief to avoid exciting this additional O, thus yielding photolytic-free measurements [41].

The NPD in this setup produces a plethora of excited states of O and O_2, resulting in a complex, but luminous and spectrally wide, emission spectrum from the oxygen plasma [42]. When probing the ground state population of O(3P) using TAPLIF, it is impossible to distinguish between the laser-induced emission from ground-state O(3P) and natural de-excitation of the excited species, as they are both spatially, temporally and spectrally overlapped. Therefore, there is a need to distinguish between LIF and plasma emission.

2.3. *Removing interfering emission*

The technique for removing plasma emission is inspired by the principles of structured illumination [34, 36, 43, 44]. When a spatially sinusoidal intensity modulation with a known frequency is applied to the exciting laser sheet, the fluorescence is

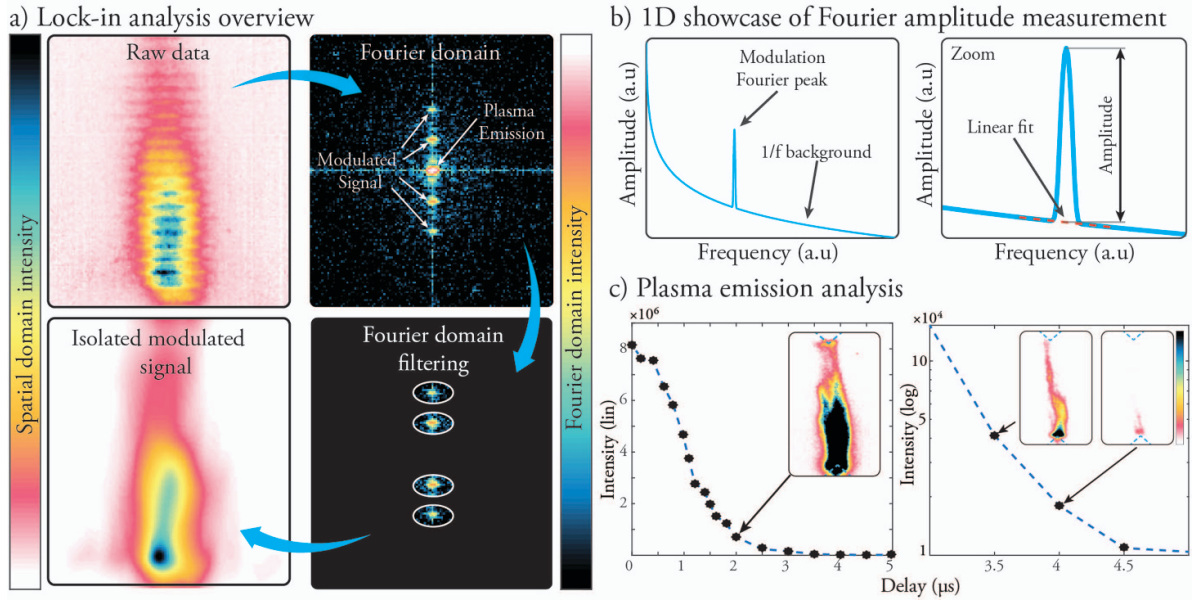

Figure 2. (a) Displays an overview of the Fourier filtering procedure for a LAC PLIF image. In the Fourier domain, five peaks are located. The centre peak, located at $f = 0$, contains the unmodulated plasma emission while the other four, two above and two below, contain the modulated laser-induced fluorescence signal. The filtering is applied around these four, resulting in an image that contains no plasma emission. (b) Displays a graphical depiction of the Fourier domain $1/f$ background and the modulation Fourier peak superimposed on top of it. (c) Displays a graph depicting the total plasma emission intensity over time, with three sample plasma emission images from 2, 3 and 4 μs delay to highlight spatial distribution of the plasma emission.

modulated with the same frequency, while the emissions from natural de-excitation will remain unmodulated. Additionally, since the excitation of O(3P) is a two-photon process, the resulting spatial fluorescence profile will follow a quadratic sinusoidal pattern. This non-linear behaviour not only modulates the signal but also enhances the total fluorescence compared to that of a homogeneous laser sheet, as the two-photon excitation amplifies local variations. For a more thorough explanation of this process we refer to Ravelid *et al* [37].

While LIF cannot be distinguished from plasma emission in the spatial domain, the applied modulation ensures that they are well-separated in the Fourier domain, enabling the use of Fourier filtering. A graphical depiction of the Fourier filtering process is illustrated in figure 2(a) Fourier filtering involves applying a bandpass filter in the Fourier domain, where each position corresponds to light with a specific modulation frequency. Light resulting from the modulated laser sheet will be located at distinct positions in the Fourier domain (forming Fourier peaks), separate from unmodulated light, and can be isolated using a spatial filter. This process is referred to as Lock-in analysis.

Furthermore, the amplitude of these Fourier peaks is directly proportional to the strength of a given modulation frequency in the data. Thus, the Fourier peaks also provide information about relative fluorescence intensity over time, and, by extension, relative O(3P) concentration (as examined in this paper). This clear distinction between, and separation of, LIF from plasma emission enables the extraction of information previously obscured by plasma emission.

Practically, employing intensified cameras, as well as slight misalignments and scattering events, lead to a reduction in modulation depth of the modulation pattern [37]. This means that the modulated signal will have a lower amplitude and form on top of a constant fluorescence offset, in addition to the plasma emission. Consequently, fluorescence power will be shifted to the Fourier domain origin and thus be indistinguishable from the plasma emission. While this reduces the total fluorescence signal that can be extracted from the Fourier domain, this reduction will be a fraction equal to the modulation depth and thus apply the same to all measurements. Furthermore, it can be compensated for by measuring the modulation depth at a time where no non-modulated emission is present.

Even though the position of most of the plasma emission in the Fourier domain is concentrated at the origin (modulation frequency 0, due to lack of modulation) random spatial variations mean that emission components are still present throughout the Fourier domain. This results in a natural Fourier amplitude spectrum from plasma emission that resembles the inverse of the frequency. This phenomenon is commonly referred to as a $1/f$ signature, reflecting the correlation between the amplitude $A(f)$ and the Fourier frequency f: $A \propto 1/f$. The Fourier peaks generated by the spatial modulation of the laser sheet appear on top of this $1/f$ background, as depicted in figure 2(b) To measure the height of these Fourier peaks above the $1/f$ background, the background level at the peak frequency must first be estimated, allowing the amplitude difference between the peak and the background to be calculated.

This amplitude extraction relies on the assumption that the Fourier peaks are distinguishable from random fluctuations in the background. However, this can be challenging to achieve

if the signal is weak (which is often the case for two-photon excitation) or if the plasma is very luminous. Nonetheless, as long as the Fourier peaks remain clearly distinguishable from the $1/f$ noise, the amplitudes can be reliably extracted, providing previously unavailable fluorescence information from the plasma afterglow.

Using Lock-in analysis to isolate the modulated signal has one drawback, however: down-sampling, a reduction in image resolution that depends on the diameter of the Fourier filter used (see supplementary materials of [37] for a full discussion). The limiting resolution before applying Lock-in analysis data was 50 μs and after applying Lock-in, using a 4×24-pixel elliptical filter, the new resolution was 2100 and 440 μm along x and y, respectively.

3. Results and discussion

3.1. Spatial O(3P) distributions

A comparison between measurements before and after applying Lock-in analysis under similar conditions was necessary to verify that applying Lock-in does not alter the measurement results. Therefore, the duration of the plasma emission was investigated to determine at which delay the plasma emission had dissipated, allowing for a valid comparison between applying and not applying Lock-in to the measurements. The total plasma emission intensity over time is graphed in figure 2(c), together with three imaging examples. The graph shows the total image intensity, on a logarithmic scale, over time. Three representative images of corresponding data are inlaid within the figure, with dashed blue lines indicating approximate electrode positions. The presented data is the average of 50 single-shots due to the significant shot-to-shot instability of the discharge, likely caused by the large discharge gap allowing a multitude of discharge paths through the gap. The total intensity of the plasma emission reached background levels at 4.5 μs. However, at 4 μs the plasma emission is very faint (even compared to the LIF intensity) and localised to just above the bottom electrode, as opposed to the data at 3.5 μs, which also has a low total intensity but is more prevalent spatially. For this reason, the data-point at 4 μs was included in the comparison, placing the cut-off point for no plasma emission to just before 4 μs.

A study of the spatial shot-to-shot variation in O(3P) fluorescence was performed, some results of which are displayed in figure 3(a). The figure displays five single-shot images of O(3P) taken 3.5 μs after the discharge, from different discharge events. Significant shot-to-shot variations are observed in all images, both in terms of discharge path and detected O(3P) distribution, indicating significant discharge-to-discharge plasma instability. To combat this randomness, and also remove data from non-spark discharges, each measurement consisted of 200 images, of which the 50 images with the highest discharge gap luminosity (a 2 mm wide and 9 mm high area between the pins) were used to form average images.

Figure 3(b) displays a comparison between not applying (top row) and applying (bottom row) Lock-in analysis to measurements, with the left column containing 50-shot averaged data and the right column containing single-shot data. These data sets were selected because they contain some plasma emission but also clearly visible modulated signal from laser-induced O(3P) fluorescence. The accumulated data shows that applying Lock-in analysis does not alter the spatial signal distribution; it follows the shape and intensity of the fluorescence modulation in the non-Lock-in image while ignoring and removing overlapping plasma emission. Note, however, that the Lock-in analysis decreases the spatial resolution of the images [37].

The ability to discriminate between fluorescence and plasma emission is more evident in the displayed single-shot data, where two islands of intensity are observed in the raw data: one in the cathode-half of the discharge gap and one in the anode half. The cathode-side island presents a higher peak intensity and larger spatial extent than the anode-side island before Lock-in is applied to the data. After applying Lock-in analysis, however, the cathode-side intensity is stronger than the anode side. This suggests that, for this single-shot image, the anode-side island intensity is laser-induced O(3P) fluorescence, while the majority of the cathode-side island intensity is due to plasma emission. The location of the plasma emission correlates well with the plasma emission data displayed in figure 2(c), showing that while there is significant plasma instability, general trends can be observed through the accumulation and averaging of data between discharges.

The results from a temporal comparison study of applying Lock-in analysis are depicted in figure 3(c). As expected, the spatial intensity distributions are maintained over time. As shown by the accumulated data in figures 3(b) and (c), more O(3P) is generally created in the cathode-half of the plasma channel than in the anode-half, with a maximum approximately 1.7 mm above the cathode tip. This distribution indicates a significant enhancement of chemical activity in the cathode-half of the discharge gap. This data correlates with the finding that plasma emission is significantly stronger in the lower half of the discharge gap as well, supporting the notion that the detected plasma emission is due to de-excitation of O^* to O(3P).

In terms of comparative simulations, Tholin and Bourdon [45]. simulated electron density resulting from a ns discharge between hyperboloid electrodes in atmospheric pressure air. After a single discharge they report an electron distribution between the pins that correlates well with our detected O(3P) distributions. According to a review article by Popov and Starikovsakaya [46], the initial production of O in a NPD is wholly due to the dissociation of O_2 through electron impact, indicating that the correlation between the electron distribution of Schmidt *et al* [22]. and the O(3P) distribution presented here is not coincidental.

3.2. Chemical lifetime comparison for data with and without Lock-in analysis

A comparison of chemical lifetimes calculated from data with and without Lock-in analysis was performed. Note that the absolute signal counts from Lock-in are naturally lower due to the filtering process, so the Lock-in data intensities were

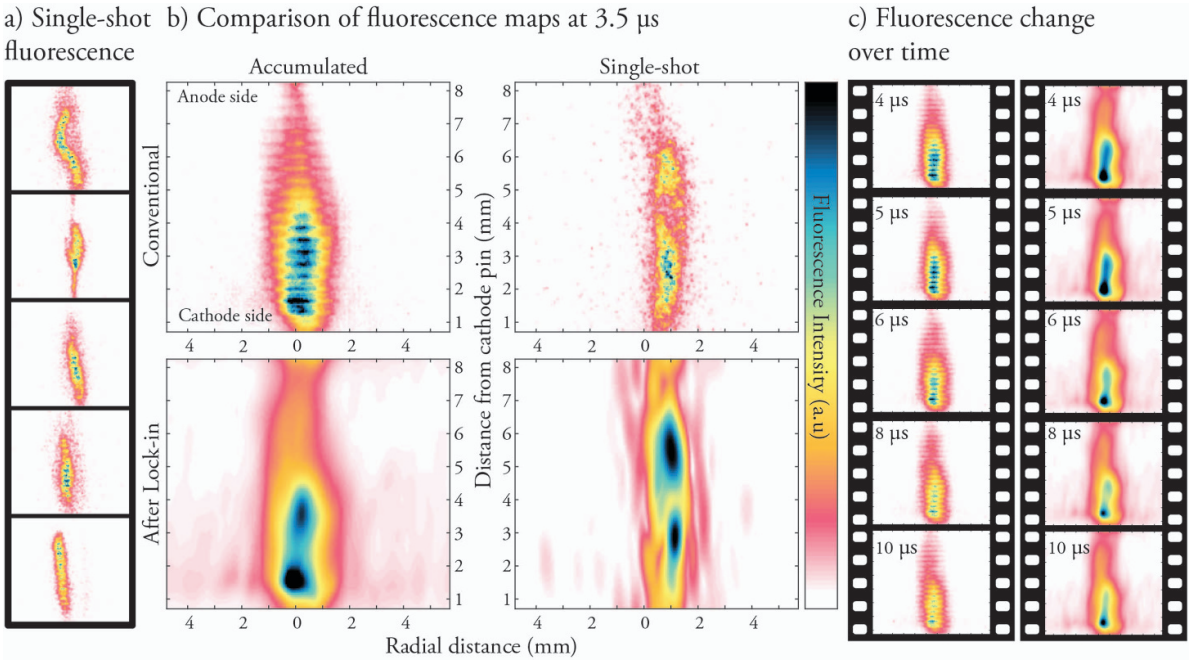

Figure 3. (a) Displays a sample of single-shot O(3P) fluorescence images, highlighting the stochasticity of the NPD. (b) Displays a comparison between not applying- and applying Lock-in analysis for both single-shot and accumulated data. The lock-in analysis both preserves the intensity distributions of O(3P) fluorescence and removes plasma emission, as is most evident in the single-shot comparison. (c) Displays a comparison similar to that in b, although only with accumulated data, at increasing delay after NPD. All are after the plasma emission has died out, showcasing the minimal effect of Fourier filtering on spatial distributions.

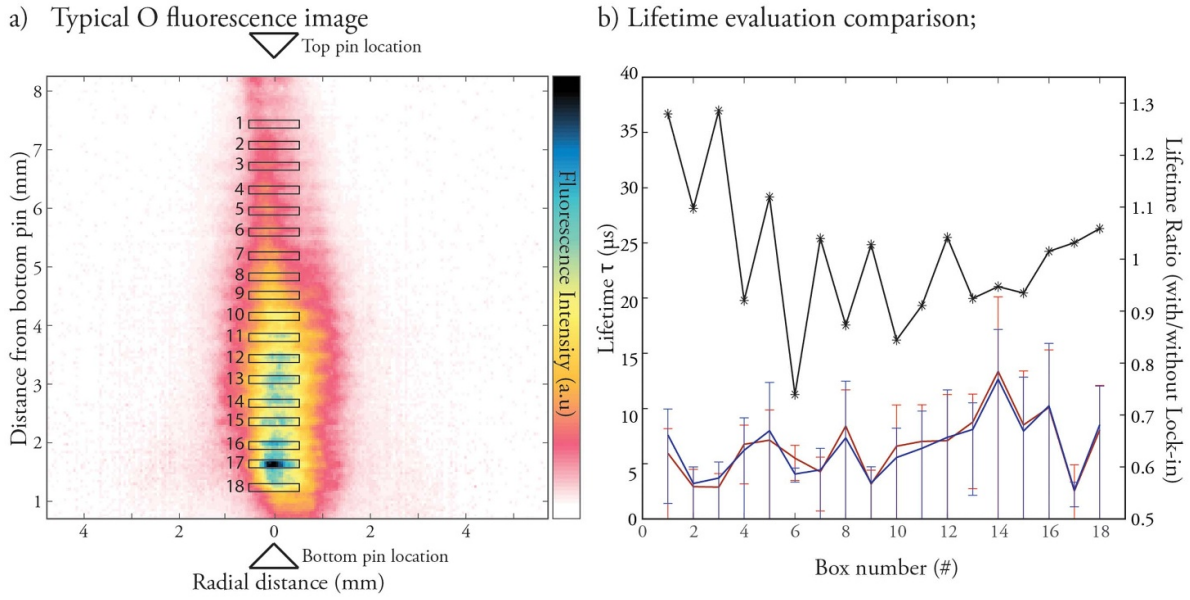

Figure 4. (a) Displays a typical O(3P) fluorescence image, as well as the approximate locations of the top and bottom electrodes. It also contains eighteen boxes (1–18) signifying the data used for preliminary O(3P) lifetime evaluations. (b) Displays the resulting lifetimes from the eighteen boxes with 95% confidence intervals. Red and blue lines represent lifetimes from data without and with Lock-in analysis performed, respectively. The black curve gives the lifetime ratio with/without for each box.

normalised to the data without Lock-in. Figure 4(a) displays a sample fluorescence image with a set of small boxes (1–18). The average intensities within these boxes are used (individually) for the calculation of chemical lifetimes. The locations of the boxes were chosen along the centreline between the pins and cover areas of high, intermediate and low intensities. The size of the boxes were 3 by 20 pixels in size.

Figure 4(b) displays the calculated lifetime for each box with (red) and without (blue) applying Lock-in. Each data point is presented with 95% confidence intervals. While there

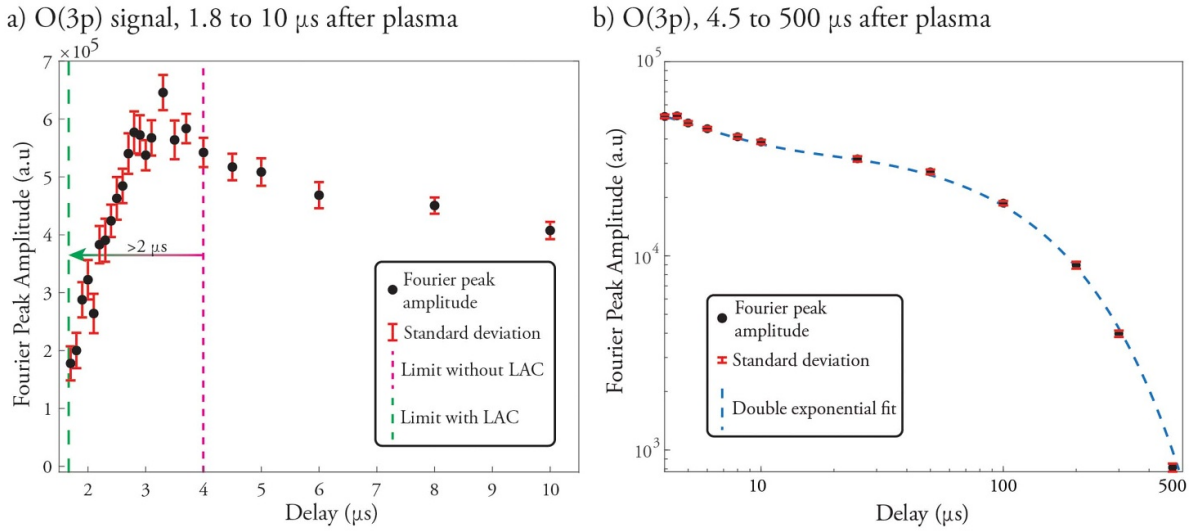

Figure 5. (a) Displays the Fourier peak amplitude, directly proportional to ground-state O(3P) concentration, between 1.7 and 10 μs after the NPD. The dashed pink line indicates where plasma emission previously limited information extraction (4 μs) and the green dashed line indicates where said limit is when utilising Lock-in analysis (1.8 μs). Due to LAC and the possibility to apply Lock-in analysis, the limit is pushed by more than 2 μs. (b) Displays the Fourier peak amplitude between 4.5 and 500 μs after discharge. The dashed blue line marks a double exponential fit to the data.

are variations from box to box, the two calculated lifetimes for each box agree very well, both falling well within the uncertainty bounds of the other. The figure also presents the individual box intensity ratio between the pre-Lock-in and post-Lock-in data (black), showing that the difference is never larger than 40% but are within 10% in the majority of cases. Applying Lock-in does, however, appear to overestimate the lifetimes by on average 2%. While this is an interesting observation, it is not considered problematic, since 2% is still well within any uncertainty bounds for the data presented here. Therefore, it is concluded that any results extracted from data using Lock-in analysis are reliable and representative, as long as the modulation Fourier peak is clearly distinguishable in the Fourier domain.

3.3. Temporal dynamics of ground state O-atom after the ns-discharge

The Lock-in analysis was then applied to O(3P) data at time delays after the discharge where the modulation Fourier peak could be identified. Figure 5 displays a plot of the modulation Fourier peak amplitude at different delays after NPD. Figure 5(a) illustrates the temporal amplitude dynamic over the first 10 μs, using data from a 65 pixel wide column centred along the vertical axis between the electrodes, with error bars signifying the standard deviation of the Fourier peak amplitudes from the set of single-shot images. The dashed lines in the figure mark the delay limit previously established in figure 2(c) (pink) and the new limit for this experiment (green), where the Fourier peak amplitude becomes indistinguishable from 1/f variations.

The data shows that the limit for how soon after discharge data can be extracted has been pushed by more than 2 μs through the use of Lock-in analysis on the data, with the first data-point now at 1.8 μs post discharge. The position of this new limit is influenced by two separate phenomena; the growth of O(3P) and the intensity of the plasma emission. The depiction of the amplitude measurement in figure 2(b) is idealised; in practice, the 1/f-background also exhibits stochastic variations (as exemplified by the grainy structure around the central peak in the Fourier domain in figure 2(a). The magnitude of these variations decrease as 1/f but also scale with total plasma emission strength, which in turn decreases exponentially with time (as seen in figure 2(c). Additionally, the O(3P) concentration is expected to be virtually zero before the discharge and then increase until it reaches its maximum value around 3.5 μs later. Consequently, at some point after discharge the stochastic variations shrink to have amplitudes similar to that of the O(3P) Fourier peak, after which distinguishing between them is possible. It should be noted, however, that employing a higher modulation frequency (thereby locating the modulation Fourier peaks farther from the Fourier domain origin, where the 1/f amplitude variation is smaller) or a more powerful laser system would push this limit even closer towards the discharge event. For this particular experimental setup, a higher modulation frequency was not possible due to space constraints for the camera position that limited imaging resolution, and thus modulation frequency.

Some work has already been done on temporal dynamics of O(3P) in this kind of plasma, though the gas mixture is almost exclusively regular air, not pure oxygen, and the pressures are generally lower. Uddi *et al* [25] compared modelling to experimental data for production of O in a flow reactor flowing air at 60 Torr through a 20 kV NPD. They report a growth phase of O, peaking around 5 μs after discharge, followed by a double exponential decay. The fast consumption dominates

until around 100 μs before being slowly consumed over tens of milliseconds. In simulations they also correlated the raise of O to the decay of electronically excited $N_2(A)$.

Popov and Starikovskaia [46] discuss a similar behaviour in air at atmospheric pressure, but on different timescales, comparing experimental data from Lo *et al* [26, 27] to modelling done by Popov [31]. They observe rapid growth until 40 ns after discharge, with a peak in O(3P) concentration at 100 ns. This dynamic is followed by an initially rapid consumption, which they attribute to a decrease in gas density due to a gas-dynamic expansion of the hot channel, rather than actual consumption of O. Thereafter, a slower consumption phase begins around 2 μs after discharge and continues for tens of microseconds.

Ju and Sun discuss the production of O(3P) extensively in their review paper [47], stating that the main production process of O(3P) during the discharge is through electron impact dissociation. After the discharge, however, the dominant process is dissociation of O_2 through collisional quenching of electronically excited N_2(B, C), as these excited states contain more energy than the dissociation energy of O_2.

When comparing these previous works to the results presented here, several observations can be made: The general temporal behaviour is the same in all three cases (fast growth followed by slow consumption), with the primary difference being the timescale on which they occur. By examining the reaction mechanism in oxygen plasma [47], some insights can be gained regarding the production of O(3P) from the stages of (1) electron impact and (2) relaxation of plasma-induced excited and ionised species. The first stage is dominated by electron impact and its duration is determined by the electron lifetime, which is typically shorter than 100 ns [46]. The available reactions are

$$e + O_2(X) \rightarrow e + 2O. \quad \text{(R1)}$$

$$e + O_2(X) \rightarrow e + O_2(a,b). \quad \text{(R2)}$$

$$e + O_2(X,a,b) \rightarrow e + 2O(3P,1D). \quad \text{(R3)}$$

The direct effect of these reactions are not observable in our data due to their very short duration. However, the electron impact processes initiate the formation of a pool consisting of electronically excited O_2(a, b), vibrationally excited $O_2(v = 1$–$41)$, O(3P, 1D), O_3, and ions (O_2+ and O−). Over the subsequent several microseconds, complex kinetics occur within this pool, accompanied by non-equilibrium energy transfer and the continuous formation of more O(3P). However, due to the very limited available data for pure O_2 plasma, it remains challenging to fully elucidate the full origin of the O(3P) peak from a pure O_2 plasma. This lack of data underscores the need for additional experimental data on O growth for advancing the O_2 plasma kinetics, limiting discussions to comparisons with air plasma.

To supplement the O fluorescence data and gauge the gas temperature, emission spectroscopy was also performed. These results are presented, together with a discussion on post-discharge gas temperature and dissociation degree of O_2, in the accompanying supplementary materials. The conclusion is that the maximum gas temperature lies in the range 5000–9000 K, due to the very high specific energy deposition. At such temperatures both O_3 and O_2 thermally dissociate much faster than they are formed, indicating a near 100% dissociation of O_2. Consequently, until the gas cools to about 5000 K it is expected to consist solely of O in various excited states.

In low-temperature gas (below 3000 K) the dissociation of O_2 only occurs during the lifetime of the free electrons, generally shorter than 100 ns [46], but in high temperature gases their lifetime can be significantly increased [48]. However, in this high-temperature regime the delayed rise in the measured ground-state O(3P) population is not necessarily indicative of continued dissociation but rather of collisional population dynamics. At temperatures above 5000 K, O–O collisions occur at rates exceeding 10^9 s^{-1}, and the energy of these collisions is often sufficient to excite atoms from low-lying excited states such as O($3p^3$P) to even higher energy levels [49], rather than de-excite them through collisional quenching. Given the narrowing energy spacing at high principal quantum numbers, this environment supports collisional excitation cycling, effectively trapping populations in excited states and delaying their return to the ground state [50, 51]. As the gas cools in the afterglow, these excitations become less probable, and a growing fraction of the atomic population relaxes into the O(3P) ground state. This mechanism likely explains the observed post-pulse increase in O(3P) density in the absence of electron collision dissociation. Additionally, the application of TALIF to excite O to the $3p^3$P state at temperatures above 5000 K will experience reduced fluorescence yield due to the additional possibility of radiation-less collisional excitation.

The maximum O concentration is reached just before 3 μs at 760 Torr in pure O_2, suggesting that the difference between this peak timing and that of Lo *et al* [26, 27], via Popov and Starikovskaia [46], is at least in part due to the absence of N_2, likely in conjunction with the previously discussed gas temperature, highlighting just how dominant the effect of N_2 is when it comes to gas kinetics. Furthermore, the results suggest that the main cause for the more rapid formation of O in air plasma, compared to pure O_2 plasma at the same pressure, is due to collision with N_2* [25, 46], which has a much higher temperature threshold for thermal dissociation. The relative delay in peak O concentration observed here would be explained by the lack of this interaction.

Another noteworthy feature is unveiled when studying the O consumption for longer than 10 μs post discharge. Figure 5(b) depicts the gradual decay of the Fourier peak amplitude between 4.5 to 500 μs on a log–log scale, using data from the same column as in figure 5(a) (Note, however, that while there is overlap, the data used in figures 5(a) and (b) are from two separate datasets and thus deviate slightly). The O(3P) consumption displays a double exponential decay, with a transition point around 50 μs. The fluorescence decay curve is displayed in figure 5(b), with a double exponential fitted to the data indicated by a dashed blue line. A very good fit is achieved ($R^2 = 0.99$), giving two decay components; a faster

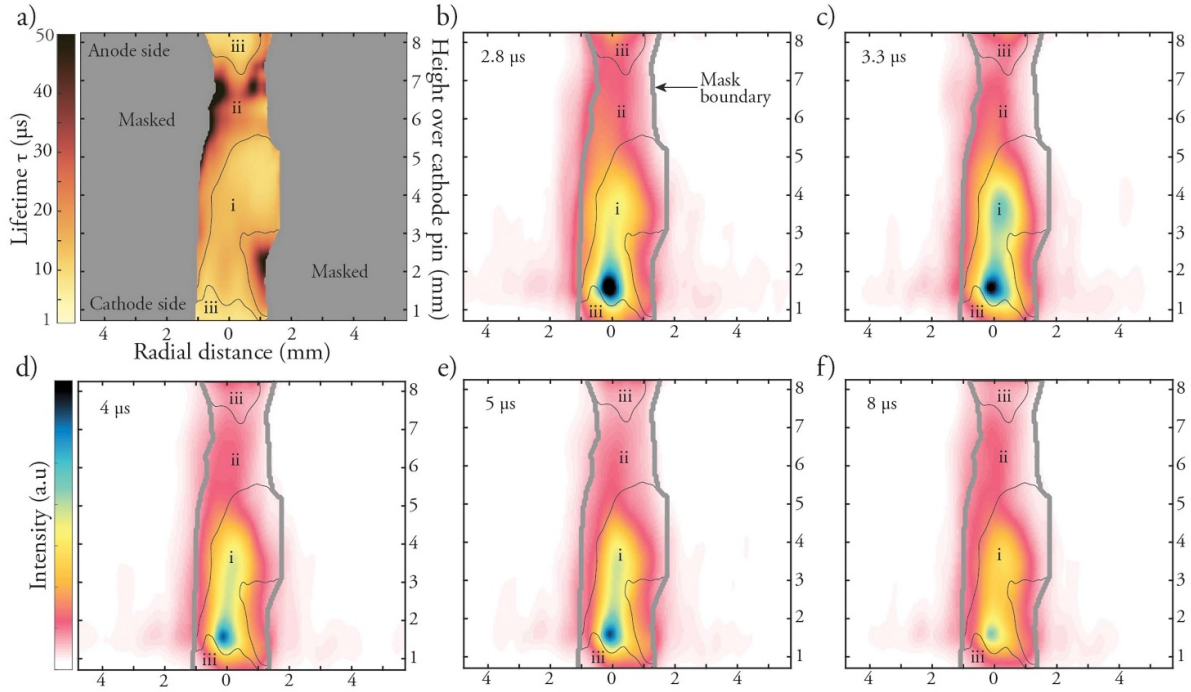

Figure 6. (a) displays a lifetime map of pixel-wise calculated lifetimes, with three areas of interest marked i–iii. The image has been masked to not display lifetime of low-signal pixels. (b)–(f) displays the fluorescence maps at different delays, with the areas of interest and mask boundaries overlaid.

decay with a lifetime of 4.5 μs and a slower with a lifetime of 110 μs, with relative amplitudes of 1:1.35 in favour if the faster consumption. For the data between 4.5 and 10 μs, this double exponential yields an average lifetime in the discharge gap of around 15 μs, agreeing well with the lifetimes shown for the same timespan in figure 4(b). The same type of behaviour is, as already mentioned, observed by Popov and Starikovskaia in the data from Lo *et al* [27, 46], albeit at much shorter timescales. The difference in timescale is likely due to the difference in gas composition and it is plausible that the fast consumption is mainly due to thermally driven expansion of the hot gas channel rather than actual consumption of O.

A possible explanation for the longer double exponential decay is in the kinetic consumption mechanics of O(3P) in the afterglow. From a kinetics point of view, the atomic oxygen concentration during the consumption phase is expected to be dominated by the following reactions, according to Nakagawa *et al* [52]:

$$O + O + M \rightleftharpoons O_2 + M \tag{R4}$$

$$O + O_2 + M \rightleftharpoons O_3 + M \tag{R5}$$

$$O + O_3 \rightarrow 2O_2. \tag{R6}$$

They report that R5 is the main channel for O consumption but that R4 cannot be neglected due to considerable dissociation of O_2 in a DBD plasma. According to the reaction rate constants given in [52], R4 has a rate constant several times higher than R5 over any relevant temperature range, further supporting that R4 cannot be neglected but it very much depends on gas temperature. For the case presented here, both R4 and R5 are initially dominated by thermal dissociation of O_2 and O_3. This effect could also explain the long O lifetime from the slow decay, compared to what was expected from Eliasson *et al* [53]. Above 5000 K no consumption of O is expected but as the gas cools below 5000 K, R4 starts to change direction, favouring formation of O_2 over thermal dissociation. As the temperature falls below 3000 K the same goes for O_3 in R5, making the consumption rate of O increase further. It is therefore plausible that the O(3P) peak observed at 3 μs coincides with the temperature where one of R4 and R5 changes direction. It should be noted that the reversal of R5 also enables R6, further enhancing the consumption rate of O.

3.4. 2D lifetime map of O consumption

So far, only the average consumption lifetime over the plasma channel has been presented. Pixel-wise lifetimes were also calculated to create a 2D map of O(3P) decay, allowing for an assessment of how the local O(3P) concentration affects its own consumption rate. Figure 6 displays six images, the first (a) displaying the 2D lifetime map of O(3P) with three regions of interest (i–iii) marked. The other five images (b)–(f) show 2D fluorescence maps from different delays after NPD. Overlaid on each image is the area contours from the lifetime map for the three regions of interest.

The three regions marked in the figure are based on general consumption lifetime but also fairly well divide the discharge gap into four distinct regions; (i) the cathode-half of the discharge gap, (ii) the anode-half of the discharge gap and (iii)

the area near the electrodes. In region (i) the O(3P) concentration is high, and the region also exhibit shorter lifetimes. Similarly, in region (ii) the O(3P) concentration is lower and the lifetimes are longer. This pattern is also observed at the edges of the discharge gap, where the behaviour mirrors that in region (ii). Thus, at first glance, lifetime appears to scale with O(3P) concentration. However, region (iii) is inconsistent with this hypothesis, as it displays lower concentrations of O(3P) but also the shortest lifetimes in the discharge gap, indicating that further investigation is required.

The arguments given by Nakagawa *et al* [52], that R4 cannot be disregarded as a source for O(3P) consumption in favour of R5, thus also explain the general correlation between O(3P) concentration and consumption rate observed in figure 6 region (i) and (ii). However, the reasoning presented by Nakagawa *et al* contradicts the behaviour observed in region (iii). This discrepancy is likely at least in part due to the electrode configuration; they utilise two spherical electrodes (one of which is coated with a dielectric) with 20 mm diameter while we use a pin-to-pin configuration. The pin-to-pin configuration is expected to produce significantly higher electric field strength near the electrodes, which in turn affects electron energy and gas composition in the volume. While a detailed analysis of this feature is beyond the scope of this publication, it could be of interest to the field as a whole to investigate this through simulations, as electrode configuration is one method to alter the chemical characteristics of processes assisted by pulsed plasma.

In pin-to-pin ns discharges, either a toroidal or cylindrical structure of hot gas can form, depending on the discharge voltage and electrode gap, as described by Dumitrache *et al* [54]. For the 9 mm gap used in this work, the expected outcome is a diffuse cylinder of hot gas in the plasma channel that cools primarily through thermal diffusion, driven by uniform energy deposition and minimal hydrodynamic motion—characteristics of the so-called diffusive regime.

However, the observed spatial distribution of O(3P) intensity and lifetime suggests a departure from perfect symmetry. Notably, regions in the upper half of the discharge channel (region ii) exhibit longer O(3P) lifetimes than those below. A plausible explanation could be a non-uniform energy deposition: if the upper half receives less deposited energy, the gas expansion (described by Starikovskaia *et al*) [46]) would decay more quickly in that region. This expansion has been proposed as the source of the fast O(3P) decay component seen in this dataset. Under this framework, the longer lifetimes in region ii can be attributed to weaker initial heating, which allows the gas to cool and stabilise earlier, shifting the decay from the fast, hydrodynamic-dominated phase to the slower, chemically limited regime. In contrast, region i, which receives more energy, continues to undergo gas expansion for a longer duration, resulting in more rapid dilution of O(3P) and consequently shorter apparent lifetimes. This spatial discrepancy is thus consistent with both the non-uniform energy deposition hypothesis and the kinetic interpretation of the dual-exponential decay behaviour.

4. Conclusion

Optical plasma diagnostics are often hindered by interfering emissions from the discharge itself, limiting their effectiveness. This work introduces LAC, a novel concept that is here used to distinguish between LIF and plasma emissions from a pin-to-pin NPD in pure oxygen gas, yielding previously unavailable information on atomic oxygen dynamics. We present the first 2D single-shot images of atomic oxygen distributions from a plasma (to the best of our knowledge). The atomic oxygen produced by the discharge was imaged at various times after the discharge using femtosecond UV laser pulses, to investigate its chemical lifetime. As part of LAC, post-processing with Fourier filtering is also applied to the data.

We show that applying Fourier filtering to the data has negligible effect on the data, and that the process accurately mitigate the effect of plasma emission. We then show that we can extract valuable information from the data directly by measuring the amplitude of the Fourier peak, at the loss of spatial resolution. This pushes the limit for how early in the afterglow data can be extracted by over 2 μs. This previously unobserved data shows that the ground-state atomic oxygen concentration grows quickly after the NPD, peaking at 3.5 μs and then being slowly consumed. Previously, only the slow consumption phase had been observed.

The finding that O(3P) peaks at 3.5 μs allows us to include more data in the lifetime fittings, resulting in more accurate lifetime calculations. Using this, we present a 2D map of chemical lifetimes of O(3P) and compare that to the O(3P) concentration maps for several different post-discharge times. The comparison suggests that the consumption rate of O(3P) largely scales with the concentration. The only outlier is the areas near the electrodes where the opposite behaviour is observed. Generally, the calculated lifetimes of O(3P) from the 30kV NPD range between 5 and 50 μs.

LAC is not only limited to O measurements but can favourably be applied to any measurement scheme that relies on multi-photon excitation, due to the aforementioned non-linear scaling of fluorescence intensity on excitation intensity. As such it is optimal for application on studies of species that are currently very difficult, including not only O(3P) but other atomic species often involved in plasma, such as H, N or C [55–57]. If only the removal of interfering emissions is needed, the LAC approach (or any variant employing structured illumination) can be applied to any imaging LIF measurement but when applied to measurements using multi-photon excitation LAC also facilitates a stronger fluorescence signal, with further amplification occurring for higher order processes. One future application could thus be to apply LAC to single-photon

transitions but instead utilising three photons for the excitation, allowing both the removal of plasma emission as well as fluorescence amplification.

Data availability statement

The data cannot be made publicly available upon publication because no suitable repository exists for hosting data in this field of study. The data that support the findings of this study are available upon reasonable request from the authors.

Acknowledgments

This research was supported by the Swedish Research Council (2021–04506, 2024-04875) Knut & Alice Wallenberg Foundation (2019.0084), the Royal Physiographic Society of Lund, the European Research Council (852394 & 803634) and the European Union Project CAIPIRINH$_3$A, under the GA number 101191768. Views and opinions expressed are however those of the authors only and do not necessarily reflect those of the European Union or CINEA. Neither the European Union nor the granting authority can be held responsible for them.

ORCID iDs

Jonas Ravelid 0000-0001-7661-5798
Jinguo Sun 0000-0001-7932-4670
Alexander A Konnov 0000-0002-8287-1592
Yupan Bao 0000-0001-8386-7109
Andreas Ehn 0000-0002-3716-8822

References

[1] Bogaerts A, Berthelot A, Heijkers S, Kolev S, Snoeckx R, Sun S, Trenchev G, Van Laer K and Wang W 2017 CO2 conversion by plasma technology: insights from modeling the plasma chemistry and plasma reactor design *Plasma Sources Sci. Technol.* **26** 5

[2] Elhambakhsh A, Long N V D, Lamichhane P and Hessel V 2023 Recent progress and future directions in plasma-assisted biomass conversion to hydrogen *Renew. Energy* **218** 12

[3] Mourão R, Marquesi A R, Gorbunov A V, Filho G P, Halinouski A A and Otani C 2015 Thermochemical assessment of gasification process efficiency of biofuels industry waste with different plasma oxidants *IEEE Trans. Plasma Sci.* **43** 3760–7

[4] Simek M and Homola T 2021 Plasma-assisted agriculture: history, presence and prospects-a review *Eur. Phys. J. D* **75** 210

[5] Petitpas G, Rollier J D, Darmon A, Gonzalez-Aguilar J, Metkemeijer R and Fulcheri L 2007 A comparative study of non-thermal plasma assisted reforming technologies *Int. J. Hydrog. Energy* **32** 2848–67

[6] Zhou L M, Xue B, Kogelschatz U and Eliasson B 1998 Nonequilibrium plasma reforming of greenhouse gases to synthesis gas *Energy Fuels* **12** 1191–9

[7] Bromberg L, Cohn D R, Rabinovich A, O'brien C and Hochgreb S 1998 Plasma reforming of methane *Energy Fuels* **12** 11–18

[8] Starikovskii A Y, Anikin N B, Kosarev I N, Mintoussov E I, Starikovskaia S M and Zhukov V P 2006 Plasma-assisted combustion *Pure Appl. Chem.* **78** 1265–98

[9] Starikovskaia S M 2006 Plasma assisted ignition and combustion *J. Phys. D: Appl. Phys.* **39** 8

[10] Grisch F, Grandin G A, Messina D and Attal-Trétout B 2011 Non-equilibrium kinetic studies of plasma-assisted combustion using laser-based diagnostics *Z. Phys. Chem.* **225** 1193–205

[11] Ju Y, Lefkowitz J K, Reuter C B, Won S H, Yang X, Yang S, Sun W, Jiang Z and Chen Q 2016 Plasma assisted low temperature combustion *Plasma Chem. Plasma Process* **36** 85–105

[12] Liu C-J, Xu G-H and Wang T 1999 Non-thermal plasma approaches in CO utilization *Fuel Process. Technol.* **58** 119–34

[13] Jeong J Y, Park J, Henins I, Babayan S E, Tu V J, Selwyn G S, Ding G and Hicks R F 2000 Reaction chemistry in the afterglow of an oxygen-helium, atmospheric-pressure plasma *J. Phys. Chem A* **104** 8027–32

[14] Jablonowski H, Sousa J S, Weltmann K-D, Wende K and Reuter S 2018 Quantification of the ozone and singlet delta oxygen produced in gas and liquid phases by a non-thermal atmospheric plasma with relevance for medical treatment *Sci. Rep.* **8** 12

[15] Goto A, Yamashita S and Tagawa M 2022 Formation of nanoscale protrusions on polymer films after atomic oxygen irradiation: changes in morphologies, masses and FT-IR spectra *Langmuir* **38** 3339–49

[16] Benson S W 1981 The kinetics and thermochemistry of chemical oxidation with application to combustion and flames *Prog. Energy Combust. Sci.* **7** 125–34

[17] Svanberg S 2003 *Atomic and Molecular Spectroscopy* 4th edn (Springer)

[18] Kwasny M and Bombalska A 2022 Applications of laser-induced fluorescence in medicine *Sensors* **22** 2956

[19] Rüttinger S, Spille C, Hoffmann M and Schlüter M 2018 Laser-induced fluorescence in multiphase systems *ChemBioEng Rev.* **5** 253–69

[20] Zare R N 2012 My life with LIF: a personal account of developing laser-induced fluorescence *Annu. Rev. Anal. Chem.* **5** 1–14

[21] Ruchkina M, Raveesh M, Dominguez A, Bood J and Brackmann C 2023 Simultaneous quantitative imaging of H and O atoms in premixed turbulent flames using femtosecond two-photon laser-induced fluorescence *Opt. Express* **31** 12932

[22] Schmidt J B, Roy S, Kulatilaka W D, Shkurenkov I, Adamovich I V, Lempert W R and Gord J R 2017 Femtosecond, two-photon-absorption, laser-induced-fluorescence (fs-TALIF) imaging of atomic hydrogen and oxygen in non-equilibrium plasmas *J. Phys. D: Appl. Phys.* **50** 1

[23] Schröter S, Bredin Jôme, Gibson A R, West A, Dedrick J P, Wagenaars E, Niemi K, Gans T and O'Connell D 2020 The formation of atomic oxygen and hydrogen in atmospheric pressure plasmas containing humidity: picosecond two-photon absorption laser induced fluorescence and numerical simulations *Plasma Sources Sci. Technol.* **29** 105001

[24] Tserepi A D, Wurzberg E and Miller T A 1997 Two-photon-excited stimulated emission from atomic oxygen in rf plasmas: detection and estimation of its threshold *Chem. Phys. Lett.* **265** 297–302

[25] Uddi M, Jiang N, Mintusov E, Adamovich I V and Lempert W R 2009 Atomic oxygen measurements in air and air/fuel nanosecond pulse discharges by two photon laser induced fluorescence *Proc. Combust. Inst.* **32** 929–36

[26] Lo A, Cessou A, Boubert P and Vervisch P 2014 Space and time analysis of the nanosecond scale discharges in atmospheric pressure air: I. Gas temperature and vibrational distribution function of N_2 and O_2 *J. Phys. D: Appl. Phys.* **47** 115201
[27] Lo A, Cessou A and Vervisch P 2014 Space and time analysis of the nanosecond scale discharges in atmospheric pressure air: II. Energy transfers during the post-discharge *J. Phys. D: Appl. Phys.* **47** 115202
[28] Lanier S, Bowman S, Burnette D, Adamovich I V and Lempert W R 2014 Time-resolved temperature and O atom measurements in nanosecond pulse discharges in combustible mixtures *J. Phys. D: Appl. Phys.* **47** 11
[29] Popov N A 2007 The effect of nonequilibrium excitation on the ignition of hydrogen-oxygen mixtures *High Temp.* **45** 261–79
[30] Popov N A 2011 Fast gas heating in a nitrogen-oxygen discharge plasma: I. Kinetic mechanism *J. Phys. D: Appl. Phys.* **44** 285201
[31] Popov N A 2016 Pulsed nanosecond discharge in air at high specific deposited energy: fast gas heating and active particle production *Plasma Sources Sci. Technol.* **25** 5
[32] Ehn A, Bood J, Li Z, Berrocal E, Aldén M and Kristensson E 2017 FRAME: femtosecond videography for atomic and molecular dynamics *Nat. Publ. Group* **6** e17045
[33] Bao Y, Dorozynska K, Stamatoglou P, Kong C, Hurtig T, Pfaff S, Zetterberg J, Richter M, Kristensson E and Ehn A 2021 Single-shot 3D imaging of hydroxyl radicals in the vicinity of a gliding arc discharge *Plasma Sources Sci. Technol.* **30** 04LT04
[34] Berrocal E, Kristensson E, Richter M, Linne M and Aldén M 2008 Application of structured illumination for multiple scattering suppression in planar laser imaging of dense sprays *Exp. Fluids* **39** 1283–90
[35] Andersson D, Bao Y, Kornienko V, Popović D and Kristensson E 2024 A light-efficient and versatile multiplexing method for snapshot spectral imaging *Sci. Rep.* **14** 16116
[36] Nilsson S, Ravelid J, Park J, Cha M S and Ehn A 2024 Photofragmentation laser-induced fluorescence imaging of CH 3 by structured illumination in a plasma discharge *Opt. Express* **32** 26492
[37] Ravelid J, Kornienko V, Bood J, Kristensson E and Ehn A 2025 Light-field amplitude control for multi-photon fluorescence imaging *Opt. Express* **33** 11192
[38] Rahman K A, Athmanathan V, Slipchenko M N, Roy S, Gord J R, Zhang Z and Meyer T R 2019 Quantitative femtosecond, two-photon laser-induced fluorescence of atomic oxygen in high-pressure flames *Appl. Opt.* **58** 1984
[39] Niemi K, Gathen V S-V D and Döbele H F 2005 Absolute atomic oxygen density measurements by two-photon absorption laser-induced fluorescence spectroscopy in an RF-excited atmospheric pressure plasma jet *Plasma Sources Sci. Technol.* **14** 375–86
[40] Shu Z, Popov N, Starikovskaia S, Popov N A and Starikovskaia S M 2024 Absolute calibration of the ratio of Xe/O two-photon absorption cross-sections for O-TALIF applications *Plasma Sources Sci. Technol.* **33** 025019
[41] Kulatilaka W D, Gord J R, Katta V R and Roy S 2012 Photolytic-interference-free, femtosecond two-photon fluorescence imaging of atomic hydrogen Opt. Lett. **37** 3051–3
[42] Rezaei F, Abbasi-Firouzjah M and Shokri B 2014 Investigation of antibacterial and wettability behaviours of plasma-modified PMMA films for application in ophthalmology *J. Phys. D: Appl. Phys.* **47** 085401
[43] Mishra Y N, Kristensson E, Koegl M, Jönsson J, Zigan L and Berrocal E 2017 Comparison between two-phase and one-phase SLIPI for instantaneous imaging of transient sprays *Exp. Fluids* **58** 9
[44] Kristensson E, Ehn A, Bood J and Aldén M 2015 Advancements in Rayleigh scattering thermometry by means of structured illumination *Proc. Combust. Inst.* **35** 3689–96
[45] Tholin F and Bourdon A 2013 Simulation of the stable 'quasi-periodic' glow regime of a nanosecond repetitively pulsed discharge in air at atmospheric pressure *Plasma Sources Sci. Technol.* **22** 8
[46] Popov N A and Starikovskaia S M 2022 Relaxation of electronic excitation in nitrogen/oxygen and fuel/air mixtures: fast gas heating in plasma-assisted ignition and flame stabilization *Prog. Energy Combust. Sci.* **91** 100928
[47] Ju Y and Sun W 2015 Plasma assisted combustion: dynamics and chemistry *Prog. Energy Combust. Sci.* **48** 21–83
[48] Miles J, Murray C, Ross A, Lemmer K, Russell J and Adams S 2020 Time resolved electron density and temperature measurements via Thomson scattering in an atmospheric nanosecond pulsed discharge *Plasma Sources Sci. Technol.* **29** 07LT02
[49] Vinoth S P, Evans E S, Swanson C P S, Palmerduca E and Cohen S A 2022 Evaluation of a collisional radiative model for electron temperature determination in hydrogen plasma *Rev. Sci. Instrum.* **93** 9
[50] Fernández-Menchero L, Zanna G D and Badnell N R 2016 Scaling of collision strengths for highly-excited states of ions of the H- and He-like sequences *Astron. Astrophys.* **592** :A135
[51] Glab W and Nayfeh M H 1982 Excitation and ionization of hydrogen Rydberg states in a plasma *Opt. Lett.* **7** 380–1
[52] Nakagawa Y, Kawakita T, Uchida S and Tochikubo F 2020 Simultaneous measurement of local densities of atomic oxygen and ozone in pure oxygen pulsed barrier discharge under atmospheric pressure *J. Phys. D: Appl. Phys.* **53** 135201
[53] Eliasson B, Kogelschatz U and Baessler P 1984 Dissociation of O2 in N2/O2 mixtures *J. Phys. B: At. Mol. Phys.* **17** L797–801
[54] Dumitrache C, Gallant A, Minesi N, Stepanyan S, Stancu G D and Laux C O 2019 Hydrodynamic regimes induced by nanosecond pulsed discharges in air: mechanism of vorticity generation *J. Phys. D: Appl. Phys.* **52** 364001
[55] Vankan P, Schram D C and Engeln R 2005 Atomic and molecular hydrogen densities in a plasma expansion *Plasma Sources Sci. Technol.* **14** 744–50
[56] Schneider S, Dünnbier M, Hübner S, Reuter S and Benedikt J 2014 Atomic nitrogen: a parameter study of a micro-scale atmospheric pressure plasma jet by means of molecular beam mass spectrometry *J. Phys. D: Appl. Phys.* **47** 12
[57] Grindlay G, Gras L, Mora J and deLoos-Vollebregt M T C 2008 Carbon-related matrix effects in inductively coupled plasma atomic emission spectrometry *Spectrochim. Acta B* **63** 234–43